Check for updates

High-efficiency photocatalysis in Ca–Cr doped BiFeO₃ nanoparticles *via* bandgap tuning

Anika Rahman Riya,†[a] Abrar Daiyan,†[a] Mehedi Hasan Prince,†[ab] Troyee Mitra Aishi,†[ac] Tinni Dey Prome,[a] Md. Abdullah Zubair,[d] Md. Fakhrul Islam[d] and Takian Fakhrul [ID] *[a]

The growing environmental threat posed by synthetic dye pollution has accelerated the search for effective semiconductor-based photocatalysts for scalable and sustainable wastewater treatment. This study reports the greatly enhanced visible-light photocatalytic activity of $Bi_{0.97}Ca_{0.03}Fe_{1-x}Cr_xO_3$ ($x = 0.00$, 0.01, 0.03, 0.05) nanoparticles synthesized *via* a modified sol–gel method. Structural analysis confirmed the formation of a distorted rhombohedral perovskite phase, with doping leading to reduced lattice parameters and crystallite size. The bandgap narrowed from 2.13 eV in pure BiFeO₃ (BFO) to 1.80 eV in the co-doped sample. Elemental analysis confirmed improved stoichiometric balance and reduced bismuth volatilization in the co-doped samples. Under xenon lamp illumination, methylene blue degradation reached 93% for $Bi_{0.97}Ca_{0.03}Fe_{0.95}Cr_{0.05}O_3$ at neutral pH, approaching the upper limits of reported efficiencies for BFO-based systems. The reaction followed pseudo-first-order kinetics, with the rate constant rising from 0.01358 to 0.03038 min⁻¹. Moreover, the formation of an antiferromagnetic–ferromagnetic core–shell structure in the co-doped samples is proposed to notably improve dye degradation by promoting surface charge separation and suppressing recombination. This work highlights the potential of Ca and Cr co-substituted BFO nanoparticles as high-performance, visible-light-driven photocatalysts for dye remediation under environmentally relevant pH conditions.

1 Introduction

Over the past two decades, rapid industrialization has resulted in the widespread discharge of harmful effluents into natural water bodies, posing serious risks to both ecosystems and human health.[1,2] Among these contaminants, textile dyes are particularly concerning due to their high chemical stability and resistance to biodegradation.[3] In response, significant research efforts have focused on developing cost-effective and environmentally sustainable dye removal techniques. However, conventional methods such as adsorption, coagulation, and membrane filtration are often limited by high energy consumption, operational complexity and secondary pollutant generation.[4–6] As a result, photocatalysis using semiconducting materials has gained traction as a more sustainable alternative. Titanium dioxide (TiO₂), the most widely studied photocatalyst, is known for its low cost and chemical stability.[7–11] Yet, its wide bandgap (E_g) (~3.2 eV) restricts its activity to UV light, demanding high-energy input. On top of that, rapid electron–hole recombination and particle agglomeration hinder its photocatalytic performance, highlighting the need for more efficient and versatile materials.[12–15]

In this context, bismuth ferrite has emerged as a promising candidate due to its relatively narrow E_g (~2.2 eV), which enables effective absorption of visible light.[16,17] Its magnetic properties, arising from the breakdown of antiferromagnetic ordering, along with its chemical stability, facilitate easy recovery and reuse after degradation.[18,19] Moreover, due to its multiferroic nature, the internal electric field promotes charge separation and reduces recombination, making it ideal for photocatalytic applications.[20–22]

Despite its potential, the photodegradation efficiency of BFO remains inconsistent across studies, largely influenced by synthesis methods, surface chemistry, and pH conditions. Extensive studies have explored the effect of solution pH on BFO's photocatalytic activity, with many reporting enhanced degradation efficiencies under both acidic and basic conditions, deviating from the dye's natural pH.[23–27] The influence of pH is particularly relevant for dyes like methylene blue (MB), a persistent and carcinogenic cationic pollutant that degrades more efficiently in non-neutral environments.[23,25] In parallel, other studies have shown that compositional tuning of the

[a]Department of Materials and Metallurgical Engineering, Bangladesh University of Engineering and Technology (BUET), Dhaka, 1000, Bangladesh. E-mail: takianf@mme.buet.ac.bd

[b]Department of Materials Science & Engineering, Rensselaer Polytechnic Institute (RPI), NY, 12180, USA

[c]Department of Chemical Engineering, Northeastern University, MA, 02115, USA

[d]Department of Nanomaterials and Ceramic Engineering, Bangladesh University of Engineering and Technology (BUET), Dhaka, 1000, Bangladesh

† Anika Rahman Riya, Abrar Daiyan, Mehedi Hasan Prince, Troyee Mitra Aishi contributed equally to this work.

photocatalyst can improve degradation performance without the need for pH adjustment.[22,28–31] Incorporating suitable elements into the BFO lattice introduces charge-trapping centers that enhance carrier mobility and mitigate recombination losses.[32] For instance, Ca^{2+} doping induces structural distortions, generates oxygen vacancies, and modulates the band structure. These changes improve charge separation and photocatalytic activity.[33,34] Similarly, Cr doping introduces trap states and increases radical generation under visible light, further boosting degradation efficiency.[35] Co-substitution with both Ca and Cr enhances the magnetic properties of BFO while inducing the formation of an antiferromagnetic–ferromagnetic (AFM–FM) core–shell structure. This configuration facilitates efficient charge transport and allows for magnetic recovery of the catalyst after treatment.[26,37,38] Investigating this combined doping approach may provide valuable insights into optimizing BFO-based systems for visible-light-driven environmental remediation.

Building on this foundation, this study optimizes the photocatalytic degradation of methylene blue by tuning BFO's bandgap through targeted doping, while maintaining the solution at pH 7 to isolate compositional effects. Pure, Ca-doped, and Ca–Cr co-substituted BFO nanoparticles (NPs) with compositions $BiFeO_3$ and $Bi_{0.97}Ca_{0.03}Fe_{1-x}Cr_xO_3$ [(BCFO; $x = 0$), (BCFOCr1; $x = 0.01$), (BCFOCr3; $x = 0.03$), (BCFOCr5; $x = 0.05$)] were synthesized via the sol–gel method. Characterization included X-ray diffraction spectroscopy (XRD), scanning electron microscopy (SEM), transmission electron microscopy (TEM), UV-visible spectroscopy (UV-vis), and photocatalytic degradation tests using MB dye, were employed to investigate the structural, morphological, optical, and photocatalytic properties of the synthesized nanoparticles.

2 Experimental section

2.1 Materials

Analytical grade (AR) bismuth nitrate pentahydrate [$Bi(NO_3)_3 \cdot 5H_2O$, $\geq 99.0\%$], iron nitrate nonahydrate [$Fe(NO_3)_3 \cdot 9H_2O$, $\geq 98.0\%$], calcium nitrate tetrahydrate [$Ca(NO_3)_2 \cdot 4H_2O$, $\geq 98.0\%$], and chromium nitrate nonahydrate [$Cr(NO_3)_3 \cdot 9H_2O$, $\geq 98.0\%$] were used as precursors. Citric acid ($C_6H_8O_7$), ethylene glycol ($C_2H_6O_2$), and deionized (DI) water were employed as the chelating agent, stabilizing agent, and solvent, respectively. All chemicals were supplied by Merck.

2.2 Preparation of $BiFeO_3$ nanoparticles

The synthesis of pure and Ca–Cr co-doped BFO nanoparticles was carried out through sol–gel method, as illustrated in Fig. 1. Stoichiometric amounts of precursor nitrates and citric acid, used in a 1 : 1 molar ratio, were dissolved in deionized water and stirred at 90–95 °C for 30 minutes. Subsequently, 10 mL of ethylene glycol was added to the solution, which was then stirred at 75–85 °C for 4 hours to induce gel formation. The resulting gel was dried at 110 °C for 24 hours, ground into a fine powder, and annealed at 550 °C for 2 hours with a heating rate of 5 °C min^{-1} to obtain crystalline nanoparticles.

2.3 Characterization

X-ray diffraction (XRD) analysis of the powder samples was performed using an Empyrean PANalytical diffractometer equipped with a hybrid PIXcel3D detector, utilizing a Cu X-ray source with wavelengths $K\alpha_1 = 1.540598$ Å and $K\alpha_2 = 1.544426$ Å, and a scanning speed of 0.041683 s^{-1}. The morphology and microstructure of the nanoparticles were examined using a field emission scanning electron microscope (FESEM, JEOL JSM 7600F) equipped with an energy-dispersive X-ray (EDX) system. Crystallographic data were extracted from the XRD patterns through Rietveld refinement using the XPert HighScore Plus software. The microstructure of the samples were examined via Transmission Electron Microscope using Talos F200X.

The photocatalytic response of the nanoparticles was evaluated using an in-house-designed photochemical reactor rig. The bandgap of the samples was investigated using a UV-Vis spectrophotometer (LAMBDA 1050, PerkinElmer). Photodegradation of methylene blue solution was carried out with the nanoparticles as the photocatalyst, under illumination from a concentric 500 watt xenon lamp emitting photons in the 250–1800 nm range. The temperatures of the source chamber and the solution were regulated using forced air circulation and
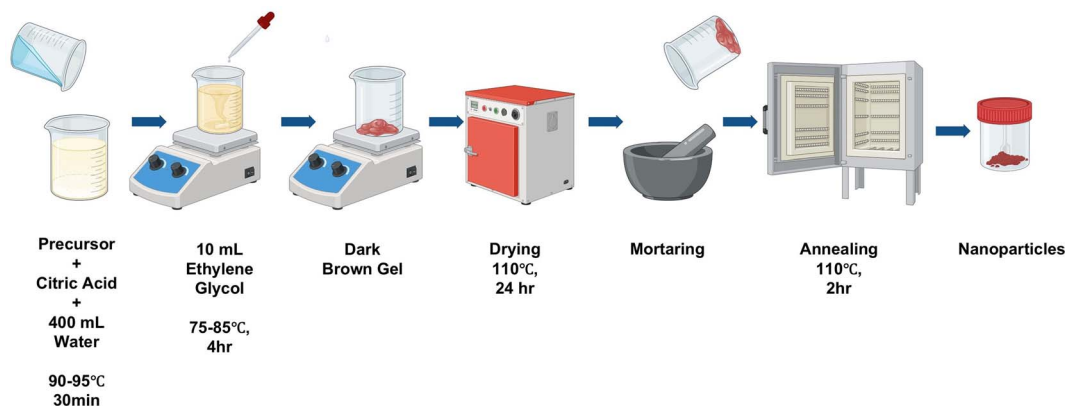

Fig. 1 Schematic diagram of the synthesis route for BFO and Ca−Cr co-substituted BFO nanoparticles.

a closed-loop water cooling system, respectively, maintaining the solution within 23–26 °C. A homogeneous nanoparticle suspension was ensured by magnetic stirring at 1000 rpm, and the pH of the solution was maintained at approximately 7. A total of 100 mg of the nanoparticle catalyst was added to 350 mL of a 3.2 ppm MB dye solution. The mixture was stirred in the dark for 30 minutes to establish adsorption–desorption equilibrium, followed by 90 minutes of illumination. Aliquots of 15 mL were collected at 10 minute intervals, and the absorption spectra of the centrifuged samples were recorded using a UV-Vis-NIR spectrometer equipped with three detector modules (TDM).

3 Result and discussion

3.1 Structural analysis

The room-temperature XRD patterns of the nanoparticles are shown in Fig. 2. The distinct doublet peaks observed at Bragg angles of 31.6° and 32°, corresponding to the (104) and (110) planes, respectively, confirm the presence of the perovskite structure of BFO with $R3c$ space group. As reported in previous studies, the synthesis of BFO is often accompanied by secondary phases such as Bi_2O_3 and $Bi_2Fe_4O_9$, denoted as α and β, respectivel.[39–41] The α phase appears as a minor peak near 27° in all samples, while the Fe-rich β phase is observed only in the BCFO sample. This is likely due to the narrow stability range of BFO and the tendency for Bi^{3+} volatilization at elevated sintering temperatures.[39]

Table 1 summarizes the crystallographic parameters of the synthesized samples, including unit cell dimensions, average particle size, dislocation density, bond angles, and bond lengths. As shown in Fig. 2(b), the major diffraction peaks shift toward higher angles upon doping, indicating structural distortion. This shift is associated with a reduction in lattice parameters, unit cell volume, and crystallite size. These changes can be attributed to the smaller ionic radii of Ca^{2+} (1.00 Å) and Cr^{3+} (0.615 Å) compared to Bi^{3+} (1.03 Å) and Fe^{3+} (0.645 Å).[41–43] This observation is consistent with Vegard's law, which states that substituting larger ions with smaller ones generally leads to lattice contraction.[44] A decrease in the c-axis with smaller crystallite sizes indicates a contraction along that direction. The merging of the (104) and (110) peaks, as represented by the decreasing values of $\Delta\theta$ ($\theta_{110} - \theta_{104}$), may eventually lead to the formation of a single (200) peak in the cubic phase, suggesting a progressive structural transformation upon dopant incorporation.[45]
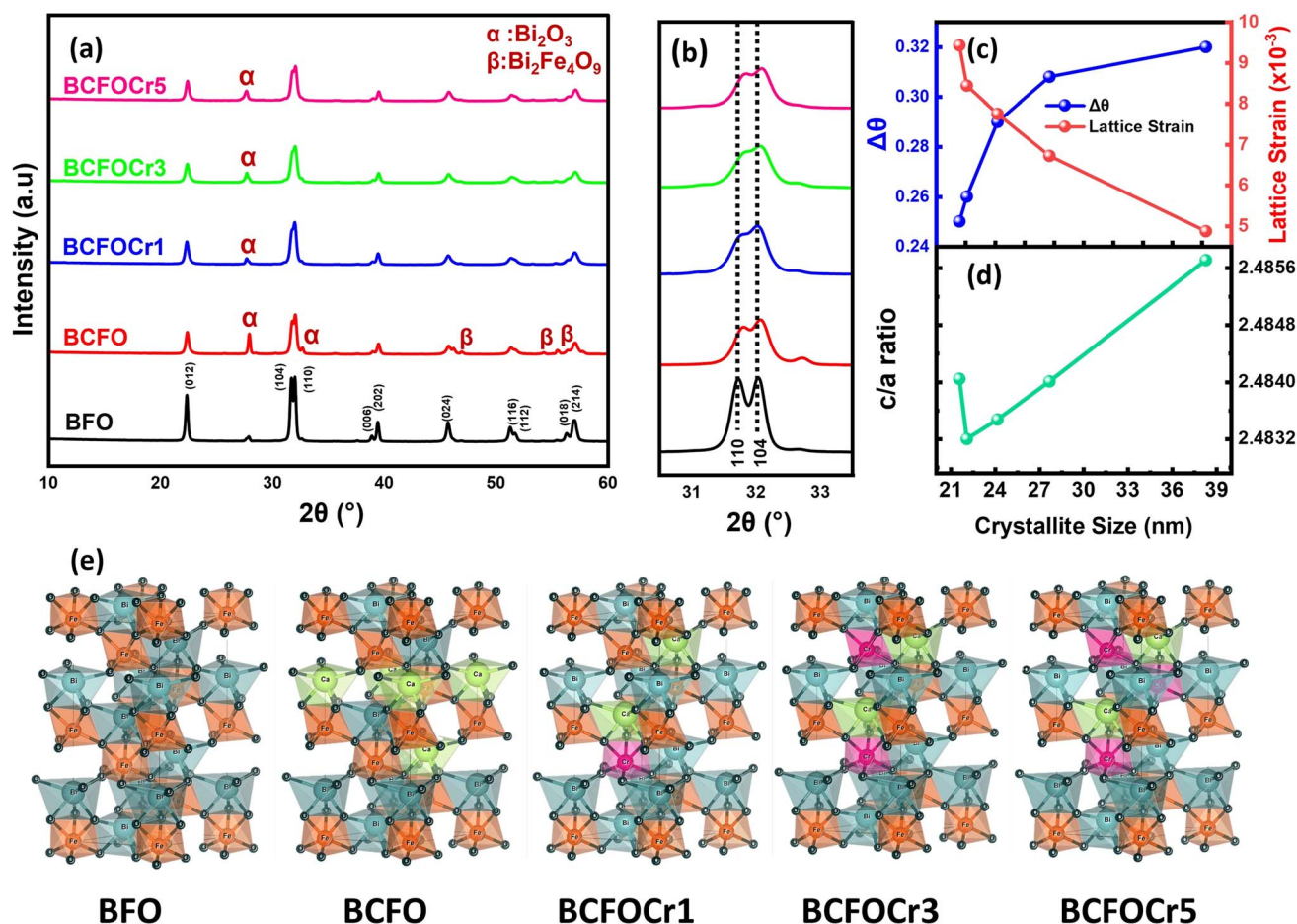

Fig. 2 (a) XRD analysis of all compositions showcasing the major peaks (b) narrow 2θ region of the major diffraction peak showing broadening upon dopant incorporation (c) Δθ and lattice strain *vs.* crystallite size (d) *c/a* ratio *vs.* crystallite size (e) crystal structures of all synthesized compositions.

Table 1 Lattice parameters, particle size, dislocation density, bond lengths and bond angles of BFO, BCFO, BCFOCr1, BCFOCr3 and BCFOCr5

Composition	Unit cell parameter (Å)	Avg. particle size (nm)	Dislocation density $\times 10^{-4}$ (nm^{-2})	Fe–O bond length (Å)	Fe–O–Fe bond angle (°)
BFO	$a = b = 5.5791, c = 13.868$	83	0.068	2.14	151.6
BCFO	$a = b = 5.5797, c = 13.860$	74	0.130	2.05	149.2
BCFOCr1	$a = b = 5.5797, c = 13.857$	71	0.172	2.05	150.7
BCFOCr3	$a = b = 5.5783, c = 13.853$	67	0.205	2.04	157
BCFOCr5	$a = b = 5.5764, c = 13.852$	61	0.214	2.02	153

Fig. 2(c) and (d) illustrate the relationship between microstrain, $\Delta\theta$, c/a ratio, and crystallite size. The c/a ratios of all doped samples are lower than that of pure BFO, which supports the observation of reduced rhombohedral distortion, eventually leading to the formation of a cubic phase.[45,46] The average crystallite sizes of the nanoparticles were calculated from XRD peak broadening using the Debye–Scherrer equation. With increasing dopant concentration, both lattice microstrain and dislocation density exhibited an upward trend, reaching their maximum values in the BCFOCr5 sample. The observed variations in microstrain and lattice parameters suggest lattice distortions induced by grain boundaries in nanocrystallites.[46,47] In contrast, the crystallite size decreased with higher doping levels, consistent with the average particle size observed in the SEM analysis.

3.2 Morphological analysis

The FESEM images shown in Fig. 3(a–e) reveal the morphological features of BFO, BCFO, BCFOCr1, BCFOCr3, and BCFOCr5 nanoparticles. All samples exhibit grain formation, consistent with the micrographs. The Ca and Cr co-substituted samples exhibit homogeneous grain structures and well-defined grain boundaries that confirm high phase purity of the nanoparticles.[48] Average particle size decreases with higher dopant concentrations. Compared to the pure BFO sample, the BCFO nanoparticles display reduced uniformity, increased surface porosity, and noticeable particle agglomeration. This results from the formation of oxygen vacancies resulting from Ca^{2+} substitution.[49] The average particle size decreases from 81 nm to 61 nm upon Ca and Cr doping and continues to decrease with higher Cr concentrations. This can be attributed to the suppression of oxygen vacancies, which limits the oxygen ion mobility and inhibits grain growth as a result.[50] The smaller particle size observed in BCFOCr5 suggests a higher surface area and enhanced adsorption capacity, both of which are expected to contribute to improved photocatalytic efficiency.[49] In the insets of Fig. 3(a–e), representative Energy Dispersive X-ray spectra (EDS) recorded from a single characteristic point are shown to illustrate elemental composition. These spectra confirm the presence of only Bi, Fe, O, Ca, and Cr. EDS spectra were collected at several points across all samples, consistently

Composition	Bi:Fe (Atomic %)
BFO	0.2:1
BCFO	0.6:1
BCFOCr1	1.1:1
BCFOCr3	1.1:1
BCFOCr5	1:1
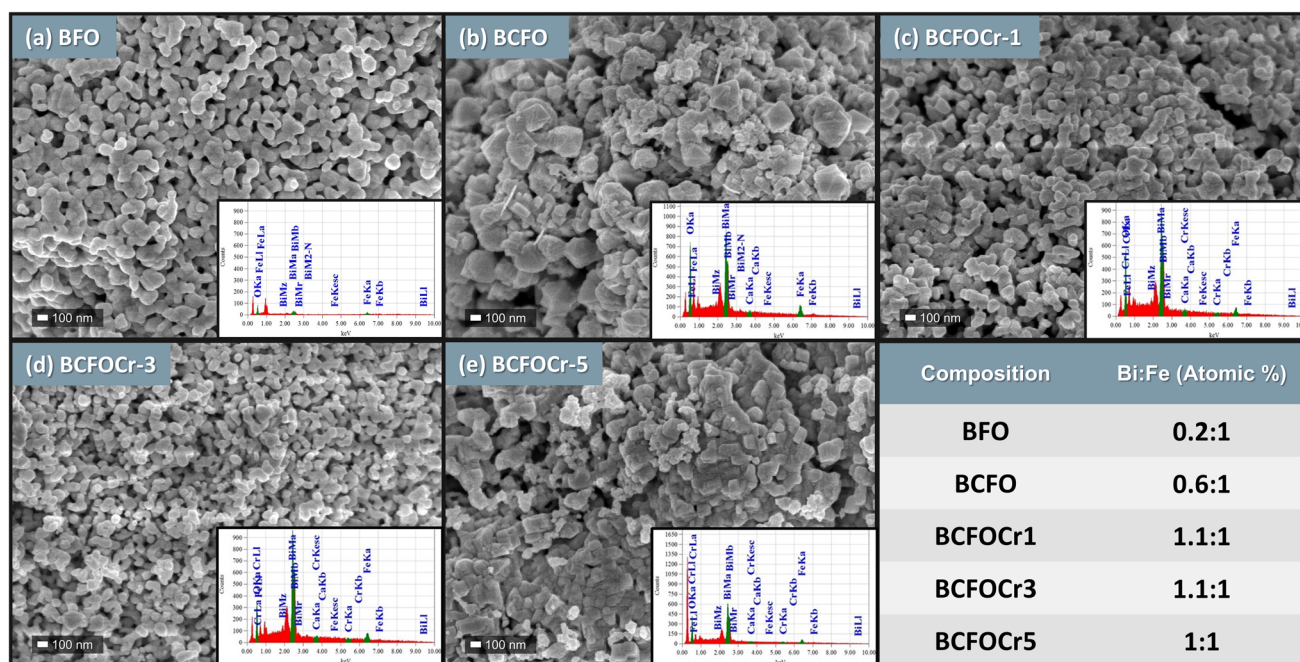
Fig. 3 SEM image of (a) BFO, (b) BCFO, (c) BCFOCr1, (d) BCFOCr3, and (e) BCFOCr5 with their insets showing representative EDS spectra from a single characteristic point.

confirming the presence of Ca and Cr and enabling a reliable determination of the Bi : Fe ratio. The multi-point EDS analysis for all compositions have been added to the SI (Fig. S1–S5).

Bismuth volatility is a well-documented challenge in bismuth-based oxide systems, including BFO.[51,52] In the present study, the undoped BFO sample was found to be significantly bismuth-deficient, as indicated by the Bi : Fe ratios in Fig. 3. However, doping with Ca and Cr notably improved the stoichiometry of the perovskite structure, with BCFOCr5 approaching the ideal stoichiometric ratio. Controlled Cr incorporation (1–5%) systematically reduced the non-stoichiometry, as verified by EDS analysis, suggesting that Cr doping helped suppress bismuth volatilization. This improved compositional balance, together with the consistent detection of Ca and Cr in the EDS spectra, supports the successful incorporation of Ca and Cr into the perovskite lattice and likely contributed to the enhanced photocatalytic performance observed in BCFOCr5.

High-resolution TEM (HRTEM) analysis was performed on the BCFOCr5 sample, the composition with the highest photocatalytic activity and most pronounced lattice strain among all the samples, to effectively capture the evolution of lattice strain. Fig. 4(a) and (b) shows the HRTEM image of BCFOCr5 nanoparticles along with the Selected Area Electron Diffraction (SAED) pattern. The polycrystalline nature of the sample, previously confirmed through XRD analysis, is further supported by the SAED pattern [Fig. 4(a)], which shows concentric rings composed of discrete bright spots. The TEM image [Fig. 4(b)] reveals lattice fringes with varying orientations, a characteristic feature of polycrystalline materials.

Each diffraction ring in the SAED pattern was indexed according to their (hkl) planes by comparing their individual d-spacing values (calculated from ring diameter) against the Powder Diffraction File (PDF) for BiFeO$_3$ (Reference code 96-100-1091). Performing the Fast Fourier Transform (FFT) algorithm on the high-resolution TEM images provided distortion free images of the lattice fringes, depicted in Fig. 4(b) insets, from which inter-planar spacing was calculated. The observed d-spacing values, $d_1 = 0.28$ nm and $d_2 = 0.39$ nm, correspond the (104) and (012) planes of BFO, respectively, using the

Table 2 Interplanar spacings (d_{hkl}) calculated from XRD for BFO and BCFOCr5, with additional HRTEM values for BCFOCr5

Composition	Plane (hkl)	d_{hkl}^{calc} (nm)	d_{hkl}^{TEM} (nm)
BFO	(104)	0.2830	—
BFO	(012)	0.3962	—
BCFOCr5	(104)	0.2810	0.2800
BCFOCr5	(012)	0.3961	0.3900

aforementioned PDF file as reference. These findings are coherent with the results obtained from the SAED pattern. The (012) and (104) planes also provide the highest intensity peaks in the XRD patterns. This, in conjunction with the TEM images, suggest that the NPs exhibit preferential orientation along these crystallographic planes.

Interplanar spacings (d_{hkl}) for selected reflections were calculated from the refined lattice parameters using the hexagonal representation of the rhombohedral $R3c$ structure, according to the relation:

$$\frac{1}{d_{hkl}{}^2} = \frac{4}{3}\frac{(h^2 + hk + k^2)}{a^2} + \frac{l^2}{c^2} \qquad (1)$$

Table 2 compares the interplanar spacings calculated from XRD-refined lattice parameters with those measured directly from HRTEM lattice fringes for BCFOCr5. For BCFOCr5, the interplanar spacings obtained from HRTEM lattice fringes agree closely with values calculated from the refined lattice parameters (0.2810 nm for (104) and 0.3961 nm for (012)). This agreement between diffraction and imaging evidence confirms that the dopant ions are incorporated into the perovskite lattice rather than forming impurity phases. The reduced d-spacings observed in BCFOCr5 by HRTEM compared to BFO (Table 2) are consistent with the lattice contraction and increased microstrain obtained from XRD analysis.

3.3 Optical properties

The band gap of the NPs was determined using the Kulbelka–Munk function applied to the UV-Vis diffuse reflectance spectra. Fig. 5(a–e) shows Tauc's plots of $(h\upsilon \times F(R))^n$ versus $(h\upsilon)$, with $n =$
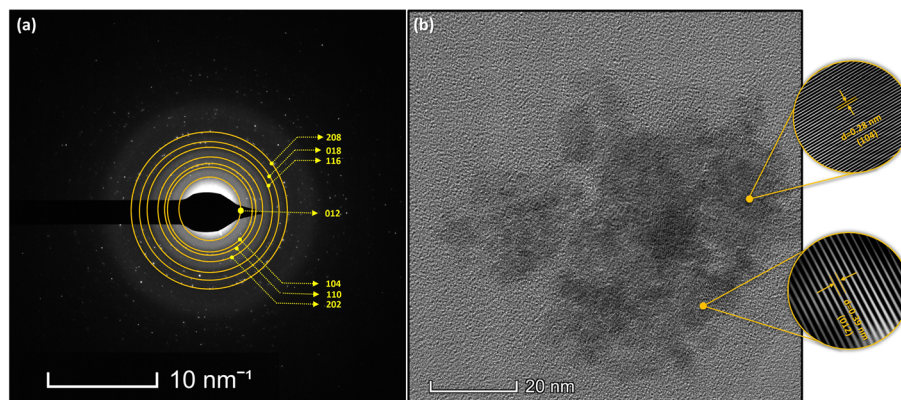
Fig. 4 (a) SAED pattern of BCFOCr5 with indexed planes (b) TEM image and corresponding lattice fringes of BCFOCr5.

2 for the direct E_g, where $F(R)$ is the Kulbelka–Munk function, h is the Plank's constant, and ν is the frequency.[53] E_g was obtained by extrapolating the linear portion of the plot to $(h\nu \times F(R))^2 =$ 0.[54] For pure BFO, E_g was 2.13 eV and decreased systematically with increased doping as shown in Fig. 5(f). This band gap arises from the energy difference between the top of the
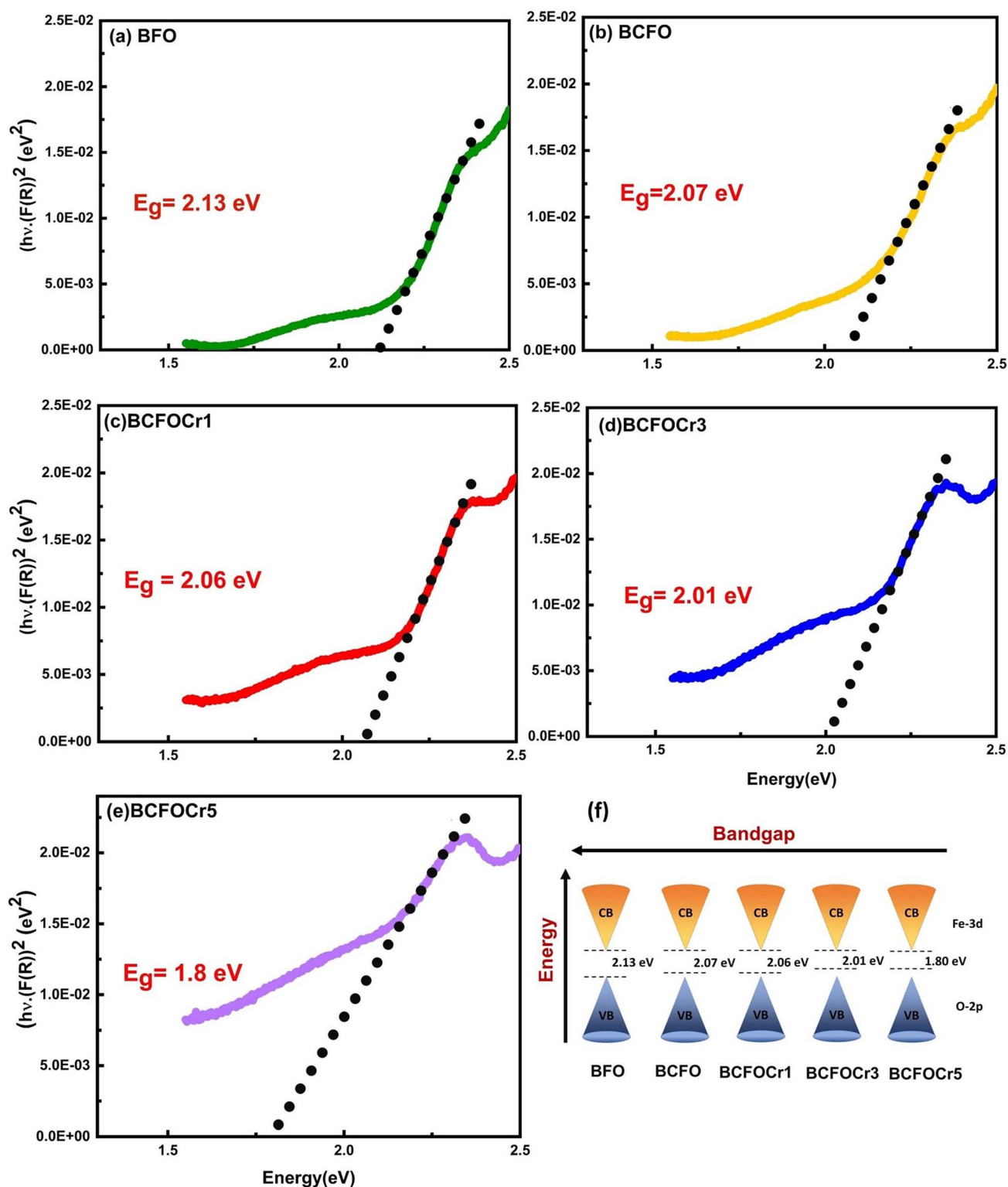

Fig. 5 Tauc plot showing direct band gap of (a) BFO, (b) BCFO, (c) BCFOCr1, (d) BCFOCr3, (e) BCFOCr5 (f) schematic illustration of the bandgap narrowing trend.

hybridized O-2p valence band and the bottom of the Fe-3d conduction band. Several factors may contribute to E_g variation, including lattice strain, defect band formation, and crystallite size effects. Previous studies have shown that the Fe–O bond length and Fe–O–Fe bond angle, as listed in Table 1, significantly influence the orbital overlap between O-2p and Fe-3d orbitals, thereby affecting the electronic band structure.[45]

Oxygen vacancy concentration increases upon doping BFO with Ca. When Ca^{2+} substitutes Bi^{3+}, a charge imbalance is introduced, leading to the formation of lattice imperfections. The Kröger–Vink notation describing this phenomenon is shown below:

$$2Ca^{2+} \xrightarrow{Bi_2O_3} 2Ca'_{Bi} + 2O_O^{\times} + V_O^{\bullet\bullet} \qquad (2)$$
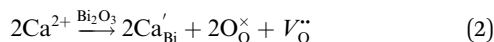
This reaction aligns with the XPS reports in our previous work on the same batch of Ca–Cr co-doped BFO samples, which confirm that the charge imbalance is primarily compensated through the formation of oxygen vacancies, rather than oxidation of Fe^{3+} to Fe^{4+}.[36] The resulting lattice imperfections introduce trap states between the conduction and valence bands, leading to a reduction in the band gap.[55] In contrast, Cr^{3+} doping does not induce additional charge imbalances since Cr and Fe share the same valence state (+3). However, E_g continues to decrease with increasing Cr content. This can be attributed to the interaction between conduction band electrons and the localized d-electrons of Cr ions at Fe sites, which leads to band gap narrowing through sp–d spin exchange interactions.[28] Additionally, Cr doping introduces defect-induced energy levels near the conduction band, which contribute to further band gap reduction, particularly in smaller particles where surface defect densities are higher.[45] Structural distortion of the FeO_6 octahedra caused by doping alters Fe–O–Fe bond angles and lengths, rearranging molecular orbitals in a way that modifies the electronic band structure and effectively narrows the band gap.[56] Lastly, the microstrain arising from non-uniform lattice distortions, dislocations, and grain boundary relaxation plays a significant role in modifying local energy levels and shifting the absorption edge.[45]

3.4 Photocatalytic activity

The photodegradation efficiency of the synthesized samples was assessed through the degradation of MB dye under illumination from a 500 watt concentric xenon lamp, emitting photons in the 250 to 850 nm range. As a cationic dye, MB typically exhibits enhanced degradation efficiency at pH values above the isoelectric point (IEP) of BFO (5.1–6.7), where surface deprotonation generates a negatively charged photocatalyst surface, thereby strengthening electrostatic attraction to the positively charged dye molecules.[23,57] To isolate the effects of compositional tuning, all experiments were conducted at a neutral pH of 7, eliminating pH as a variable.

The concentration of MB in the solution was monitored before and after photodegradation by extracting aliquots at fixed time intervals and analyzing them using a UV-Vis spectrophotometer. The absorption spectra of the MB dye solution

at various time points in the presence of suspended nanoparticles are shown in Fig. 6(a–e). Upon exposure to the xenon lamp, the characteristic blue color of the MB solution gradually faded, indicating progressive degradation of the dye and a corresponding shift in the absorption peaks.

Degradation kinetics were evaluated using a plot of $\ln\frac{C_0}{C_t}$ versus time, in accordance with the Langmuir–Hinshelwood model, confirming that the reaction follows pseudo-first-order kinetics

$$\ln\frac{C_0}{C_t} = kt \qquad (3)$$

where, C_0 is the initial concentration of the dye, C_t is the final concentration of the dye and k is the pseudo first-order reaction rate constant. Upon addition of the pure and doped BFO nanoparticles, the MB dye solution underwent noticeable discoloration, transitioning from deep blue to nearly colorless. The degradation efficiency was calculated using the following expression:

$$\text{Efficiency} = \frac{C_0 - C_t}{C_0} \times 100 \qquad (4)$$

After 90 minutes of illumination, the degradation efficiencies were found to be 71%, 72%, 76%, 78%, and 93% for BFO, BCFO, BCFOCr1, BCFOCr3, and BCFOCr5, respectively [Fig. 6(h)], indicating a significant improvement in the photocatalytic performance with increasing dopant concentration. It is worth noting that the 93% degradation efficiency in BCFOCr5 observed here is among the highest reported for BFO systems explicitly tested at neutral pH.

The corresponding reaction rate constants (k) were 0.01358, 0.01450, 0.01586, 0.01700, and 0.03038 min^{-1} for BFO, BCFO, BCFOCr1, BCFOCr3, and BCFOCr5, respectively [Table 3], reconfirming the critical role of dopant concentration in modulating photocatalytic activity. The systematically enhanced rate constants observed here are consistent with improved charge separation upon Ca–Cr doping. Although photoluminescence (PL) measurements would directly probe carrier recombination, our photocatalytic kinetics already provide clear evidence of suppressed recombination. This enhancement stems from the combined effects of band gap narrowing and particle size reduction induced by Ca and Cr co-doping. A narrower E_g enhances visible light absorption and boosts the generation of electron–hole pairs, while smaller particle sizes increase surface area, offering more active sites for redox reactions.[58,59] Doping also creates trap states that hinder charge carrier recombination, thereby improving overall efficiency. Additionally, at higher dopant levels, the formation of a core–shell structure further strengthens photocatalytic activity by establishing a localized surface electron cloud that functions as an internal electric field, promoting effective charge separation, as discussed in Section 3.6.

Under xenon lamp irradiation, the $Bi_{0.97}Ca_{0.03}Fe_{1-x}Cr_xO_3$ nanoparticles absorb photons with energies equal to or greater
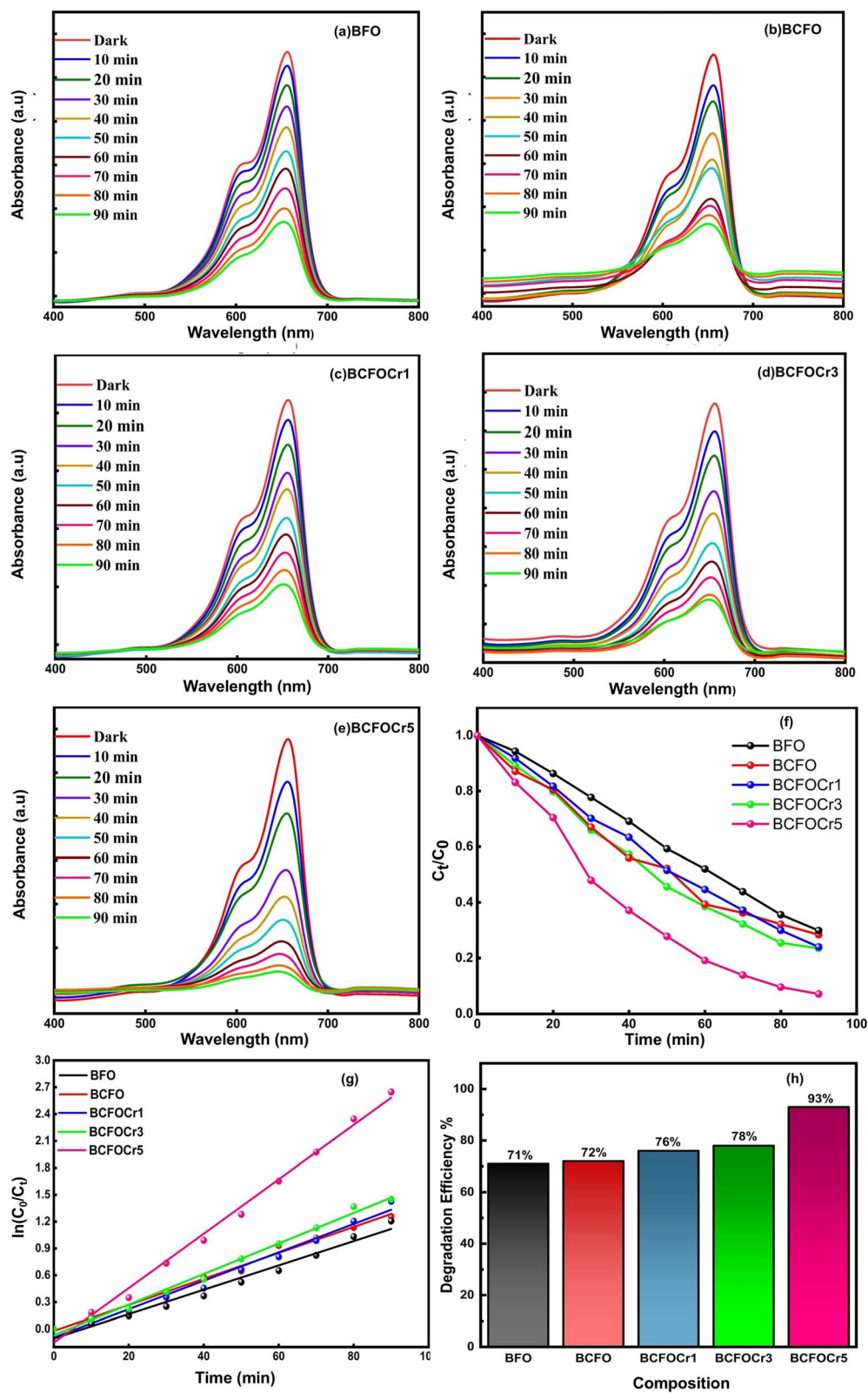
Fig. 6 UV-Vis absorption spectra of MB dye at regular time intervals for (a) BFO, (b) BCFO, (c) BCFOCr1, (d) BCFOCr3, and (e) BCFOCr5; (f) corresponding photocatalytic degradation performance, (g) linear fit plots of MB absorption, and (h) degradation efficiency.

Table 3 Band gap (E_g), dye type, degradation efficiency and rate constant (k) of BFO, BCFO, BCFOCr1, BCFOCr3, BCFOCr5

Composition	E_g (eV)	Dye	k (min^{-1})
BFO	2.13	MB	0.01358
BCFO	2.07		0.01450
BCFOCr1	2.06		0.01586
BCFOCr3	2.01		0.01700
BCFOCr5	1.80		0.03038

than its E_g [eqn (5)], leading to the generation of electron–hole pairs. These charge carriers migrate to the catalyst surface, where they participate in redox reactions that produce Reactive Oxygen Species (ROS), primarily superoxide radicals ($O_2^{\cdot-}$) *via* oxygen reduction [eqn (6)] and hydroxyl radicals ($^{\cdot}OH$) through water oxidation [eqn (7)]. The resulting ROS actively degrade dye molecules, as shown in eqn (8) and (9). Additionally, direct degradation by photogenerated holes is depicted in eqn (10).[58,59] These reactive radicals oxidize MB into carbon dioxide (CO_2) and water (H_2O), while converting nitrogen (N) and sulfur (S) heteroatoms into inorganic byproducts like nitrate, ammonium, and sulfate ions, respectively.[60] A schematic overview of this mechanism is presented in Fig. 7.
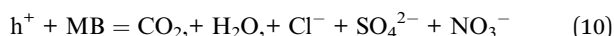
$$BCFOCr + h\upsilon = e^- + h^+ \quad (5)$$

$$O_2 + e^- = O_2^{\cdot-} \quad (6)$$

$$H_2O + h^+ = {}^{\cdot}OH \quad (7)$$

$$O_2^{\cdot-} + MB = CO_2 + H_2O + Cl^- + SO_4^{2-} + NO_3^- \quad (8)$$

$${}^{\cdot}OH + MB = CO_2 + H_2O + Cl^- + SO_4^{2-} + NO_3^- \quad (9)$$

$$h^+ + MB = CO_2, + H_2O, + Cl^- + SO_4^{2-} + NO_3^- \quad (10)$$
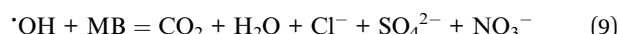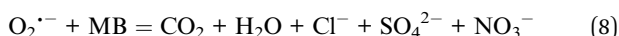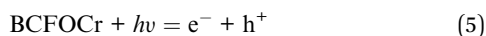
Table 4 presents a comparative analysis of pure and doped BFO systems, summarizing their synthesis methods, E_g, pH conditions, and photocatalytic efficiencies. As seen, the co-doped BCFOCr5 sample exhibits the highest degradation efficiency (93%) under explicitly neutral pH. This performance was achieved solely through compositional tuning, without any external pH adjustment. Since MB degradation tends to accelerate under alkaline conditions, further optimization of pH could potentially yield complete dye removal.

3.5 Relationship between magnetic and photocatalytic properties

Fig. 8(a) displays the magnetic properties of the Ca and Cr co-substituted BFO nanoparticles. In a previous study, we demonstrated that co-substitution resulted in the formation of an antiferromagnetic–ferromagnetic (AFM–FM) core–shell structure in BFO, resulting in enhanced magnetization.[36] This structural configuration remains highly relevant to the present work, as the electron-dense, polarized surface of the ferromagnetic shell promotes enhanced photocatalytic degradation by facilitating greater electron–hole pair generation while suppressing their recombination through surface trap states.[22] The trapped photogenerated charge carriers subsequently participate in redox reactions, leading to the formation of ROS that degrade dye molecules into less harmful byproducts. This phenomenon, along with the core–shell structure, is illustrated in Fig. 7 and 8(b). This AFM–FM core–shell structure, previously demonstrated to enhance magnetization in our earlier work,[36] therefore establishes a direct connection between the modified magnetic state and improved photocatalytic efficiency.

Furthermore, the increased saturation magnetization significantly improves the potential for magnetic separation, which is a key factor in enabling the recovery and reuse of photocatalysts for cost-effective, sustainable, and scalable applications.[28,61–63] Previous studies have already demonstrated the reusability of BFO catalysts. For example, Soltani *et al.* reported that pure BFO retained its degradation efficiency in
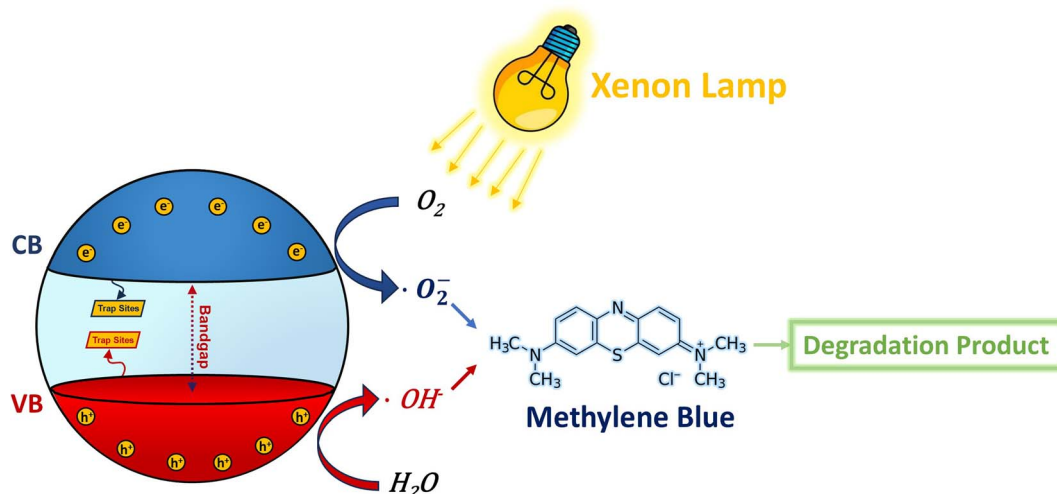
Fig. 7 Schematic diagram of photocatalytic degradation mechanism of MB dye.

© 2025 The Author(s). Published by the Royal Society of Chemistry

Table 4 Comparative study of synthesis method, E_g dye type, pH, degradation efficiency and k different compositions of BFO nanopaticles

| Composition	Synthesis method	E_g (eV)	Dye	pH	Degradation efficiency	Ref.
BFO	Sol–gel	2.36	MB	7	69% in 240 min	64
BFO	Hydrothermal	2.12	MB	7–8	52% in 180 min	65
BFO	Sol–gel	2.02	MB	7	81% in 150 min	24
BFO	Sol–gel	2.02	MB	3	99% in 90 min	24
BFO	Hydrothermal	2.08	MB	6.8	45% in 90 min	66
BFO	Sono-synthesis	2.17	MB	6	10% in 90 min	26
BFO	Sono-synthesis	2.17	MB	2.5	100% in 80 min	26
BFO	Sol–gel	1.91	MB	6.7	100% in 150 min	23
BFO	Sol–gel	1.91	MB	11	100% in 30 min	23
BFO	Biotemplate	Not reported	MB	8–10	96% in 180 min	67
BFO	Sol–gel	1.8	MB	8	98.49% in 120 min	68
BFO	Solgel	1.8	MB	4.3	96.2% in 180 min	68
BFO	Sol–gel	2.38	MB	Not reported	58% in 240 min	22
$Bi_{0.9}Gd_{0.1}FeO_3$	Sol–gel	2.32	MB	Not reported	94% in 240 min	22
$Bi_{0.95}Sr_{0.05}Fe_{0.99}Cr_{0.01}O_3$	Sol–gel	1.86	MB	Not reported	92.9% in 90 min	31
$Bi_{0.95}Sm_{0.05}Fe_{0.8}Mn_{0.2}O_3$	Sol–gel	1.52	MB	Not reported	65% in 180 min	28
$Bi_{0.85}Sm_{0.15}Fe_{0.95}Cr_{0.05}O_3$	Sol–gel	1.96	MB	Not reported	99.16% in 90 min	29
$Bi_{0.90}Gd_{0.05}Sm_{0.05}FeO_3$	Solvo-thermal	1.96	MB	2.24	95% in 40 min	30
$Bi_{0.95}Y_{0.05}FeO_3$	Biotemplate	2.05	MB	8	94.5% in 180 min	69
$Bi_{0.985}Sn_{0.015}FeO_3$	Sol–gel	1.94	MB	Not reported	99% in 120 min	70
$Bi_{0.9}Gd_{0.1}FeO_3$	Hydrothermal	1.18	MB	Not reported	97% in 180 min	71
Co doped BFO	Polyol	Not reported	MB	3.5	35.06% in 120 min	72
BCFOCr5	Sol–gel	1.77	MB	7	93% in 90 min	Present work
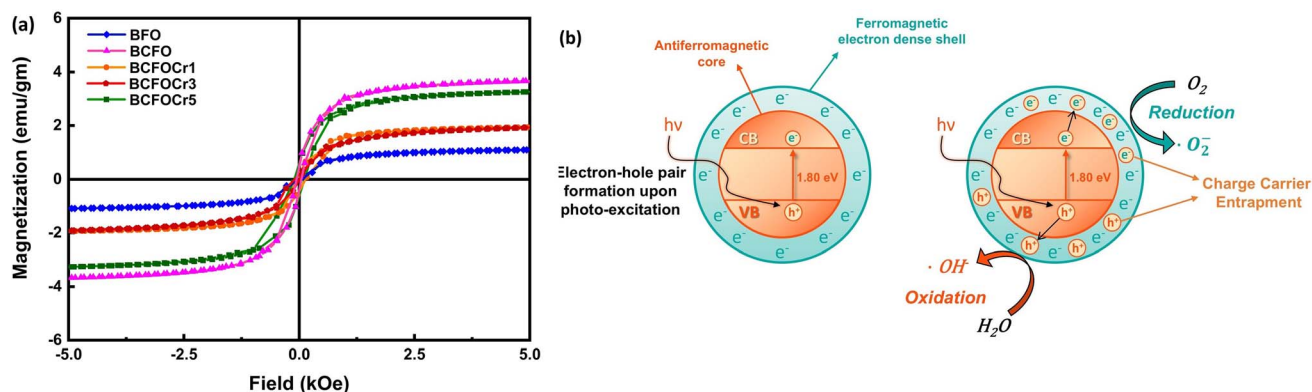
Fig. 8 (a) RT M−H hysteresis loops of the samples (b) schematic illustration of the AFM−FM core−shell structure of BCFOCr5 with photoexcitation-induced electron−hole pairs with enhanced degradation upon charge carrier entrapment in the electron dense shell.

rhodamine B dye without any loss of activity across four cycles,[25] while Jhansi *et al.* observed unchanged structural, morphological, and dye degradation properties of BFO nanoparticles across three cycles in MB.[23] Based on these findings, it is reasonable to anticipate that the magnetically recoverable Ca–Cr co-substituted BFO nanoparticles explored in this study hold strong potential for practical reuse in wastewater treatment applications,[73] even though a detailed recycling study lies beyond the scope of the present work.

4 Conclusion

In this study, BFO nanoparticles were successfully modified through Ca and Cr co-doping using a sol–gel synthesis approach, resulting in a marked improvement in the photo-degradation performance under visible light. Structural and compositional analysis confirmed successful dopant incorporation and improved stoichiometry, particularly through the suppression of bismuth volatilization. Optical characterization revealed a systematic bandgap narrowing from 2.13 eV to 1.8 eV in the most heavily doped sample. The optimized composition, BCFOCr5, exhibited a degradation efficiency of 93 percent for MB at neutral pH, one of the highest reported for BFO-based systems under such conditions. Our work also explores the relationship between magnetism and photocatalytic activity, which offers deeper insight into charge separation mechanisms and the material's multifunctional potential. In particular, the formation of an AFM−FM core−shell structure further enhances

charge separation and suppresses recombination, thereby contributing to the observed photocatalytic efficiency. These findings demonstrate that Ca and Cr co-substitution provides a promising route to improve BFO's photocatalytic performance in environmentally realistic settings. From a green-chemistry standpoint, the Ca–Cr co-doped BFO system reduces corrosive inputs by operating at neutral pH, improves energy efficiency through visible-light activation, and offers potential for magnet-assisted recovery and reuse, thereby lowering secondary waste.[64] Future work should assess reusability, long-term stability, and performance in real wastewater systems to evaluate practical implementation.

Conflicts of interest

The authors declare no conflict of financial interests or personal relationships that could have influenced the research presented in this paper.

Data availability

The data that support the finding of this study are available from the corresponding author upon reasonable request.

Supplementary information: multi-point EDS spectra for all compositions (BFO, BCFO, and Ca–Cr co-doped BiFeO$_3$ variants) used in this study. See DOI: https://doi.org/10.1039/d5ra06225j.

Acknowledgements

References

1 H. M. Solayman, Md. A. Hossen, A. A. Aziz, N. Y. Yahya, K. H. Leong, L. C. Sim, M. U. Monir and K.-D. Zoh, *J. Environ. Chem. Eng.*, 2023, **11**, 109610.

2 S. Fatima, S. I. Ali, M. Z. Iqbal and S. Rizwan, *Catalysts*, 2020, **10**, 367.

3 T. K. Dixit, S. Sharma and A. S. K. Sinha, *Mater. Sci. Semicond. Process.*, 2020, **123**, 105538.

4 B. S. Rathi and P. S. Kumar, *Environ. Pollut.*, 2021, **280**, 116995.

5 J.-Q. Jiang, *Curr. Opin. Chem. Eng.*, 2015, **8**, 36–44.

6 S. Hube, M. Eskafi, K. F. Hrafnkelsdóttir, B. Bjarnadóttir, M. Á. Bjarnadóttir, S. Axelsdóttir and B. Wu, *Sci. Total Environ.*, 2019, **710**, 136375.

7 R. Chandra and M. Nath, *J. Water Process Eng.*, 2020, **36**, 101266.

8 J. Jeon, D. H. Kweon, B. J. Jang, M. J. Ju and J. Baek, *Adv. Sustainable Syst.*, 2020, **4**, 2000197.

9 I. Arora, H. Chawla, A. Chandra, S. Sagadevan and S. Garg, *Inorg. Chem. Commun.*, 2022, **143**, 109700.

10 J. Yu, H. Yu, B. Cheng, M. Zhou and X. Zhao, *J. Mol. Catal. A: Chem.*, 2006, **253**, 112–118.

11 J. Yu, X. Zhao and Q. Zhao, *Thin Solid Films*, 2000, **379**, 7–14.

12 H. Dong, G. Zeng, L. Tang, C. Fan, C. Zhang, X. He and Y. He, *Water Res.*, 2015, **79**, 128–146.

13 S. M. Tichapondwa, J. P. Newman and O. Kubheka, *Phys. Chem. Earth, Parts A/B/C*, 2020, **118–119**, 102900.

14 R. Krakowiak, J. Musial, P. Bakun, M. Spychała, B. Czarczynska-Goslinska, D. T. Mlynarczyk, T. Koczorowski, L. Sobotta, B. Stanisz and T. Goslinski, *Appl. Sci.*, 2021, **11**, 8674.

15 C. B. Anucha, I. Altin, E. Bacaksiz and V. N. Stathopoulos, *Chem. Eng. J. Adv.*, 2022, **10**, 100262.

16 S. Irfan, L. Li, A. S. Saleemi and C.-W. Nan, *J. Mater. Chem. A*, 2017, **5**, 11143–11151.

17 K. A. McDonnell, N. Wadnerkar, N. J. English, M. Rahman and D. Dowling, *Chem. Phys. Lett.*, 2013, **572**, 78–84.

18 T. Cadenbach, V. Sanchez, K. Vizuete, A. Debut, C. Reinoso and M. J. Benitez, *Molecules*, 2024, **29**, 3592.

19 X. Wang, Y. Lin, Z. C. Zhang and J. Y. Bian, *J. Sol-Gel Sci. Technol.*, 2011, **60**, 1–5.

20 N. Arti, R. Gupta, S. P. Singh, R. Walia, V. Kumar and V. Verma, *J. Alloys Compd.*, 2022, **908**, 164602.

21 M. M. Rhaman, M. A. Matin, M. a. A. Mamun, A. Hussain, M. N. Hossain, B. C. Das, M. A. Hakim and M. F. Islam, *J. Mater. Sci.: Mater. Electron.*, 2020, **31**, 8727–8736.

22 S. Mohan, B. Subramanian, I. Bhaumik, P. K. Gupta and S. N. Jaisankar, *RSC Adv.*, 2014, **4**, 16871–16878.

23 K. Jhansi and P. Swaminathan, *J. Electron. Mater.*, 2025, **54**, 485–498.

24 M. Verma, A. Kumar, V. K. Thakur, A. Maurya, S. Kumar, S. Singh and S. K. Srivastav, *J. Sol-Gel Sci. Technol.*, 2025, **113**, 356–373.

25 T. Soltani and M. H. Entezari, *Chem. Eng. J.*, 2013, **223**, 145–154.

26 T. Soltani and M. H. Entezari, *J. Mol. Catal. A: Chem.*, 2013, **377**, 197–203.

27 N. D. M. Ridzuan, N. H. M. Kaus, M. A. S. M. Lazim, T. Kobayashi, R. Adnan, M. Z. Othman and M. H. M. Kassim, *J. Environ. Chem. Eng.*, 2020, **8**, 104152.

28 S. Irfan, Y. Shen, S. Rizwan, H. Wang, S. B. Khan and C. Nan, *J. Am. Ceram. Soc.*, 2016, **100**, 31–40.

29 M. T. Kebede, S. Devi, V. Dillu and S. Chauhan, *J. Mater. Sci. Eng. B*, 2022, **283**, 115859.

30 P. R. Vanga, R. V. Mangalaraja and M. Ashok, *J. Mater. Sci.: Mater. Electron.*, 2016, **27**, 5699–5706.

31 T. M. Aishi, presented in part at 2023, *IEEE International Conference on Telecommunications and Photonics (ICTP)*, Dhaka, Bangladesh, 2023.

32 B. Tripathi, S. Chauhan, M. Kumar, M. Sahni, P. Gupta, P. C. Sati, S. Singh, D. Agarwal and R. C. Singh, *J. Mater. Sci.: Mater. Electron.*, 2022, **33**, 16856–16873.

33 F. Fahim, M. Ramzan, B. Basha, A. U. R. Khan, M. N. Akhtar, S. U. R. Khan, A. M. Al-Mohaimeed, W. A. Al-Onazi, A. Rehman and M. S. Al-Buriahi, *Ceram. Int.*, 2025, **51**, 26411–26421.

34 V. Balasubramanian, S. Kalpana, R. Anitha and T. S. Senthil, *Mater. Sci. Semicond. Process.*, 2024, **182**, 108732.

35 J. A. Khan, I. Ahmad, M. Jawaid, A. Meraj, S. Mukhtar, J. Lakkakula and I. Uddin, *J. Iran. Chem. Soc.*, 2025, **22**, 337–347.

36 A. Daiyan, M. H. Prince, T. M. Aishi, A. R. Riya, Md. F. Islam, Md. A. Zubair and T. Fakhrul, *Ceram. Int.*, 2025, **51**, 35506.

37 T. Zhou, X. Su, O. Y. Mei, R. Min, G. Zhang and M. Zhang, *SSRN Elec. J.*, 2024, 5007912.

38 Y. Bian, G. Zheng, W. Ding, L. Hu and Z. Sheng, *RSC Adv.*, 2021, **11**, 6284–6291.

39 M. Valant, A.-K. Axelsson and N. McN. Alford, *Chem. Mater.*, 2007, **19**, 5431–5436.

40 A. Feroze, M. Idrees, D.-K. Kim, M. Nadeem, S. A. Siddiqi, S. F. Shaukat, M. Atif and M. Siddique, *J. Electron. Mater.*, 2017, **46**, 4582–4589.

41 S. M. Selbach, T. Tybell, M.-A. Einarsrud and T. Grande, *J. Solid State Chem.*, 2010, **183**, 1205–1208.

42 P. Hartman and H. Chan, *Pharm. Res.*, 1993, **10**, 1052–1058.

43 A. Kumar and K. L. Yadav, *J. Mater. Sci. Eng. B*, 2010, **176**, 227–230.

44 A. R. Denton and N. W. Ashcroft, *Phys. Rev. A*, 1991, **43**, 3161.

45 P. S. V. Mocherla, C. Karthik, R. Ubic, M. S. R. Rao and C. Sudakar, *Appl. Phys. Lett.*, 2013, **103**, 022910.

46 S. M. Selbach, T. Tybell, M.-A. Einarsrud and T. Grande, *Chem. Mater.*, 2007, **19**, 6478–6484.

47 W. Qin, T. Nagase, Y. Umakoshi and J. A. Szpunar, *Philos. Mag. Lett.*, 2008, **88**, 169–179.

48 R. Verma, A. Chauhan, N. Neha, K. M. Batoo, R. Kumar, M. Hadhi and E. H. Raslan, *Ceram. Int.*, 2020, **47**, 3680–3691.

49 F. Wang, D. Chen, N. Zhang, S. Wang, L. Qin, X. Sun and Y. Huang, *J. Colloid Interface Sci.*, 2017, **508**, 237–247.

50 J. Tiburcio, E. Sacari, J. Chacaltana, J. Medina, F. Gamarra, C. Polo, E. Mamani and A. Quispe, *Energies*, 2023, **16**, 786.

51 T. Fakhrul, S. Tazlaru, L. Beran, Y. Zhang, M. Veis and C. A. Ross, *Adv. Opt. Mater.*, 2019, **7**, 1900056.

52 T. Fakhrul, S. Tazlaru, B. Khurana, L. Beran, J. Bauer, M. Vančík, A. Marchese, E. Tsotsos, M. Kučera, Y. Zhang, M. Veis and C. A. Ross, *Adv. Opt. Mater.*, 2021, **9**, 2100512.

53 G. Hussain, I. Ahmed, A. U. Rehman, M. U. Subhani, N. Morley, M. Akhtar, M. I. Arshad and H. Anwar, *J. Alloys Compd.*, 2022, **919**, 165743.

54 H. B. Sharma, Ng. B. Singh, K. N. Devi, J. H. Lee and S. B. Singh, *J. Alloys Compd.*, 2013, **583**, 106–110.

55 W. A. Wani, S. Kundu, K. Ramaswamy and H. Venkataraman, *J. Mater. Sci. Eng. B*, 2021, **271**, 115299.

56 P. C. Sati, M. Arora, S. Chauhan, M. Kumar and S. Chhoker, *J. Phys. Chem. Solids*, 2013, **75**, 105–108.

57 J. Ćirković, A. Radojković, D. L. Golić, N. Tasić, M. Čizmić, G. Branković and Z. Branković, *J. Environ. Chem. Eng.*, 2020, **9**, 104587.

58 A. Haruna, I. Abdulkadir and S. O. Idris, *Heliyon*, 2020, **6**, e03237.

59 Z. Hu, D. Chen, S. Wang, N. Zhang, L. Qin and Y. Huang, *J. Mater. Sci. Eng. B*, 2017, **220**, 1–12.

60 I. Khan, K. Saeed, I. Zekker, B. Zhang, A. H. Hendi, A. Ahmad, S. Ahmad, N. Zada, H. Ahmad, L. A. Shah, T. Shah and I. Khan, *Water*, 2022, **14**, 242.

61 Y. Huo, Y. Jin and Y. Zhang, *J. Mol. Catal. A: Chem.*, 2010, **331**, 15–20.

62 S. Irfan, Z. Zhuanghao, F. Li, Y.-X. Chen, G.-X. Liang, J.-T. Luo and F. Ping, *J. Mater. Res. Technol.*, 2019, **8**, 6375–6389.

63 X. Li, H. Zhou, R. Qian, X. Zhang and L. Yu, *Chin. Chem. Lett.*, 2025, **36**, 110036.

64 H. Cao, X. Xiao, X. Zhang, Y. Zhang and L. Yu, *Chin. Chem. Lett.*, 2025, **36**, 110924.

65 M. Sakar, S. Balakumar, P. Saravanan and S. Bharathkumar, *Nanoscale*, 2016, **8**, 1147–1160.

66 M. Othman, I. Mallek-Zouari, H. Akrout and N. T. Mliki, *Ceram. Int.*, 2022, **49**, 10580–10587.

67 R. Dhanalakshmi, M. Muneeswaran, P. R. Vanga, M. Ashok and N. V. Giridharan, *AIP Conf. Proc.*, 2015, **1665**, 130014.

68 N. S. A. Satar, R. Adnan, H. L. Lee, S. R. Hall, T. Kobayashi, M. H. M. Kassim and N. H. M. Kaus, *Ceram. Int.*, 2019, **45**, 15964–15973.

69 N. N. Mharsale, P. S. More, Y. B. Khollam, S. F. Shaikh, A. M. Al-Enizi and S. R. Gadakh, *J. Phys. Chem. Solids*, 2024, **192**, 112049.

70 H. A. M. Azmy, N. A. Razuki, A. W. Aziz, N. S. A. Satar and N. H. M. Kaus, *J. Phys. Sci.*, 2017, **28**, 85–103.

71 S. Chakraborty, N. Chakraborty, S. Mondal and M. Pal, *Ceram. Int.*, 2022, **48**, 37253–37263.

72 F. Sharmin and M. A. Basith, *J. Alloys Compd.*, 2022, **901**, 163604.

73 A. Paliwal, R. Banu, R. Ameta and S. C. Ameta, *J. Appl. Chem.*, 2017, **6**, 967–975.